International Journal of Heat and Mass Transfer 238 (2025) 126488

Contents lists available at ScienceDirect

International Journal of Heat and Mass Transfer

journal homepage: www.elsevier.com/locate/ijhmt

Suppression strategy for metal droplet overlapping fusion defects caused by droplet impact dynamics under coaxial shielding gas

Yi Zhou, Jun Luo, Lin Su, Lehua Qi *

School of Mechanical Engineering, Northwestern Polytechnical University, Xi'an 710072, China

ARTICLE INFO

Keywords:
Coaxial shielding gas
Oxidation
Droplet deposition
Droplet overlapping
Metal micro-droplet deposition manufacturing

ABSTRACT

High-precision droplet overlapping under coaxial shielding gas is a prerequisite for automated and lightweight metal micro-droplet deposition manufacturing. Unfortunately, the opening shielding environment exposes metal droplets directly to the atmosphere. Droplet overlapping fusion quality would be affected due to the coupling effects of impact dynamics, thermodynamics, and oxidation. In this study, based on experiments and theoretical modeling of molten droplet impact dynamics, a strategy to suppress droplet overlapping fusion defects under coaxial shielding gas was proposed for the first time. Results show that at lower shielding gas rates, molten droplet retraction, recoil, and oscillation would weaken or vanish due to the oxide film's self-limiting effect. This limits the improved model's accuracy in predicting the droplet spreading factor in lower shielding gas supply rates. The weakened droplet dynamic behaviors at low shielding gas supply rates would magnify the length and height defects of droplet overlapping, which is particularly evident at a small printing step distance. Finally, a quality mapping for different printing parameters is established, effectively suppressing overlapping defects and ensuring fusion quality through metallurgical bonding. This work could provide a solid evidence base and theoretical guidance for high-quality metal micro-droplet deposition manufacturing under an opening shielding environment.

1. Introduction

Metal micro-droplet deposition manufacturing (MDDM) has gained significant attention for its low energy consumption, broad material availability, and high cost-efficiency [1]. Applications include electronic packaging [2,3], circuit printing [4,5], metal prototyping [6,7], plasmonic device manufacture [8,9], and structural repair [10]. This technology creates three-dimensional parts by depositing and fusing molten metal droplets onto a substrate, point by point and layer by layer [11,12]. To accommodate automated and lightweight manufacturing, using coaxial shielding gas (CSG) for low-oxygen protection is an ideal way [13,14], which enables rapid material supply and overcomes fabrication size limitations [15]. During MDDM, small metal droplets with slow ejection velocities require careful shielding gas management to avoid airflow disturbances impacting droplet trajectories. However, a low shielding gas supply rate risks oxidizing the molten metal, forming oxide skins on droplet surfaces and altering droplet deposition and overlapping behavior. It is challenging to guarantee metal droplet overlapping accuracy and fusion quality in CSG-based MDDM.

The overlapping fusion defect of metal droplets in an opening environment is influenced by the coupling effects of impact dynamics, thermodynamics, and oxidation. Droplet impact dynamics occur in two conditions: droplet-to-substrate and droplet-to-droplet. The investigation on the droplet-to-substrate impact behavior mainly focuses on droplet impact deformation [16,17], heat and mass transfer, and non-isothermal solidification [18,19]. The precise control of droplet deposition morphology has been achieved at present. For the droplet-to-droplet impact behavior, Xu et al. [20] developed a temperature model for adjacent droplet interfaces to predict droplet remelting behaviors. Qi et al. [21] established a horizontal overlapping model to optimize printed line morphology. Yi et al. [22] identified solidification ripples as barriers to fusion, suggesting reduced substrate thermal conductivity to minimize defects. Dou et al. [23] analyzed droplet coalescence dynamics to control landing errors during droplet overlapping. Despite these advances, most researches were done in a closed environment with an inert gas glove box providing low-oxygen protection, while the external air hardly affects the droplet deposition. In an opening environment, metal droplets are more susceptible to oxidation.

* Corresponding author.
E-mail address: qilehua@nwpu.edu.cn (L. Qi).

https://doi.org/10.1016/j.ijheatmasstransfer.2024.126488
Received 2 September 2024; Received in revised form 28 October 2024; Accepted 20 November 2024

Droplet fluid properties would change due to the oxide film formed, causing existing theories on droplet deposition dynamics and overlapping quality controlling strategies to be inapplicable.

The influence of oxidation on MDDM processes has not yet been reported. Some studies in thermal spraying involving oxidized metal droplet deposition may offer useful Refs. [24–26], though they differ from metal droplet printing. Xu et al. [26] studied the effect of oxidation on the impact dynamics of eutectic gallium alloy droplets, defining an equivalent Weber number to predict the droplet's maximum spreading factor. McGuan et al. [28], based on Pasandideh-Fard's energy conservation model [27], introduced a simplified model to predict the maximum spreading factor of oxidized gallium alloy droplets. It is shown that the maximum spreading factor for oxidized droplets is proportional to the 0.5 power of the Weber number, compared to 0.25 power for pure droplets. Yang et al. [24] analyzed aluminum droplet spreading, rebound, and splash on PTFE substrates at different oxygen concentrations, revealing oxidation increases viscous dissipation and inhibits rebound. Current literature focuses on predicting oxidized droplet characteristic parameters. Moreover, the Weber number often reaches dozens to hundreds [29], making oxidation effects insignificant due to the strong inertia effect. However, the Weber number in MDDM is below 10, while oxidation has a more significant effect on droplet deposition. A more thorough experimental and theoretical analysis is needed to clarify the droplet impact dynamic and guarantee the metal droplet overlapping fusion quality.

This work focuses on CSG-based MDDM, aiming to develop a strategy to suppress metal droplet overlapping fusion defects. A CSG supply system was employed to control droplet oxidation, while high-speed photography captured droplet-to-substrate and droplet-to-droplet impact dynamics. Through experiments and theoretical modeling, an improved model was developed to predict the droplet maximum spreading factor at a low Weber number. The evolution of droplet spreading, recoil, oscillation, and overlapping behaviors was analyzed. Furthermore, a quality mapping and parameter control strategy for droplet overlapping were proposed, effectively suppressing overlapping defects and ensuring fusion quality. This work may offer theoretical guidance for high-quality metal droplet forming in opening environments.

2. Experimental methods

2.1. Deposition setup and procedure

Fig. 1 shows the schematic diagram of the CSG-based MDDM system. The experimental system mainly consists of a temperature control subsystem, a metal droplet on-demand ejection subsystem, a droplet deposition control subsystem, a cooling recycling subsystem, and an inert gas supply subsystem. Each subsystem is working as detailed below.

The temperature control subsystem includes a temperature controller (Shimax, Japan), a thermocouple (Type K), and a heater to melt the tin alloy blocks in the crucible. The metal droplet on-demand ejection subsystem is composed of an industrial personal computer (IPC, GoldSun, China), a Programmable Multi-Axis Controller (PMAC, Delta Tau, America), a signal amplifier (Coremorrow XE-505.00, China), a piezoelectric ceramic (Coremorrow, China), a vibration rod, and a nozzle. During droplet ejection, the IPC directs the PMAC to generate a 0~5 V signal, which is amplified 12 times by the signal amplifier and applied to the piezoelectric ceramic. In response, the piezoelectric ceramic converts the electrical energy of the received signal into mechanical energy, inducing a tiny perturbation in the liquid metal via the vibration rod connected below it. This results in molten metal being squeezed from the nozzle to form a droplet of several hundred microns.

Concurrently with droplet ejection, the droplet deposition control subsystem adjusts the droplet deposition position. This subsystem includes the IPC, the PMAC, motor drivers, a 3D motion platform, and a substrate. The IPC and PMAC generate motion signals, controlling the platform and substrate to translate and lift through motor drivers. Since piezoelectric ceramics could suffer irreversible performance degradation at temperatures above 150 °C, the cooling recirculation subsystem continuously circulates water around the ceramics to maintain an optimal operating temperature.

In addition, the inert gas supply subsystem provides both shielding gas and backpressure gas for droplet ejection. Shielding gas is introduced through an inlet at the top of the heater, where internal gas distribution channels ensure its uniform distribution. This forms a coaxial shielding gas that is directed towards the nozzle, creating a low-oxygen environment in its vicinity. Simultaneously, inert gas flows into the crucible through a backpressure gas inlet located at its top, providing the necessary backpressure to extrude waste metal liquid.

The experimental research was conducted by a self-developed prototype machine of CSG-based MDDM. Detailed information on the

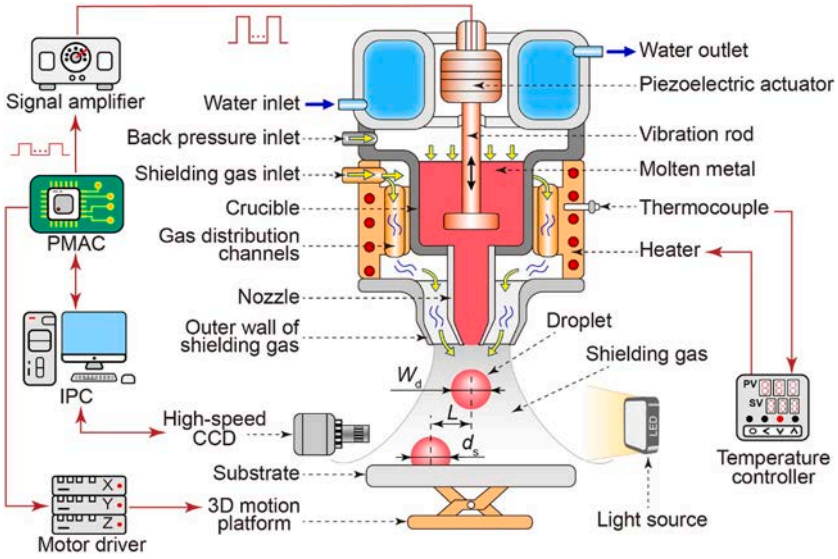

Fig. 1. Schematic diagram of the CSG-based MDDM system.

prototype machine is shown in the Supporting File.

2.2. Experimental materials and preparation

Sn99.3-Cu0.7 alloy blocks were used as the ejection material, with gold-clad boards serving as the substrate for droplet deposition. Tin alloys exhibit excellent wettability with gold cladding due to the formation of intermetallic compounds at high temperatures, which helps prevent the tin alloy droplets from rebounding from the substrate. Argon was used as the inert shielding gas to protect the droplets from oxidation during deposition. The properties of the experimental materials involved are listed in Table 1.

Prior to the experiment, the alloy block surface was finely polished to remove any oxidized film, thereby mitigating the impact of oxidation on the experimental process. Once the alloy blocks were positioned in the crucible, inert gas was supplied continuously for 5 min at a flow rate of 2 L/min through both the backpressure inlet and the shielding gas inlet to purge any residual air from the system. Before activating the heater, the backpressure gas was shut off, and the shielding gas supply rate was reduced to 0.5 L/min to prevent air backflow into the device during heating.

2.3. Characterization methods

The dynamic processes of droplet deposition and overlapping were captured using a high-speed CCD (ix-speed 220, Britain) at a frame rate of 10,000~11,500 fps. The solidification morphology and element distribution of droplets were examined by scanning electron microscope (SEM, Zeiss EVO 10, Germany) equipped with an energy dispersive spectrometer (EDS). An image analysis software, ImageJ, was employed to measure droplet characteristic dimensions.

3. Results and discussion

3.1. Metal droplet initial conditions under shielding gas

According to the previous study [34], variations in deposition distance can create two distinct shielding gas flow patterns. By controlling the deposition distance to the critical point where these two flow patterns transition, gas disturbances during droplet ejection can be minimized. In this study, the transition point for the two flow patterns was determined to be approximately 2.5 mm, and this deposition distance was subsequently maintained throughout the experiments. The pulse amplitude, pulse width, and crucible temperature were adjusted to 3.8 V, 339 μs, and 623 K, respectively, to ensure the formation of a single droplet.

The droplet initial states, such as length, width, circularity, and velocity of droplets, relative to the shielding gas supply rate before the droplet impacts the substrate are illustrated in Fig. 2. When the shielding gas supply rate is low (below 0.8 L/min), the droplet exhibits a sharp, tapered tail in their initial morphology. Previous researches by Xu et al. [26], Li et al. [35], and McGuan et al. [28] have attributed this tapered tail to oxidization. Specifically, the self-limiting oxide film on the metal jet surface restricts the release of surface energy during the jet longitudinal pull-off and necking, forming a poorly circularity droplet with a

Table 1
Properties of materials used in the experiment (at 573 K).

Properties	Sn99.3-Cu0.7	argon
Density (kg·m^{-3})	$\rho_m = 6900$	$\rho_g = 1.6228$
Dynamics viscosity (Pa·s)	$\mu_m = 1.95 \times 10^{-3}$ [30]	$\mu_g = 2.125 \times 10^{-5}$
Surface tension coefficient (N·m^{-1})	$\sigma = 0.56$	–
Melting point (K)	$T_m = 500$ [31]	–
Thermal conductivity (W·m^{-1}·K^{-1})	$k_m = 30$ [32]	$k_g = 0.017$
Latent heat of fusion (J/kg)	$H_f = 44{,}375$ [31]	–
Specific heat (J·kg^{-1}·K^{-1})	$C_m = 243$ [33]	$C_g = 521$

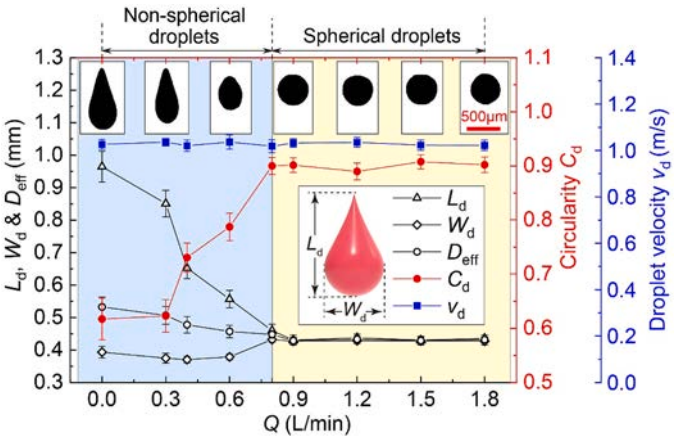

Fig. 2. Initial physical conditions of droplets at different shielding gas supply rates.

tapered tail. The presence of this tapered tail significantly increases the droplet's length while slightly reducing its width. Conversely, when the shielding gas supply rate exceeds 0.8 L/min, the weakening of oxidation leads to a reduction in droplet length, making it comparable to the width and gradually approaching a spherical shape. Furthermore, the droplet's initial velocity remains almost stable at ~1 m/s, regardless of changes in the shielding gas supply rate. This is attributed to the fact that the initial Weber number of the metal jet at the nozzle outlet (which is the ratio of the jet inertial force to the surface tension defined as $\rho_m v_{jet}^2 d_{nozzle}/\sigma$, where v_{jet} is the jet's initial velocity at the nozzle outlet and d_{nozzle} is the nozzle diameter) is of the order of magnitude ~20, indicating that the jet breakup process governed by the inertial force. The calculated correlation coefficient between the droplet's initial velocity v_d and the shielding gas supply rate Q is ~0.21, indicating a weak relationship between the two variables. Therefore, it could be assumed that the droplet's initial velocity is unchanged throughout the deposition experiment.

Most studies on droplet deposition are based on an ideal spherical droplet assumption. However, oxidation could induce irregular metal droplet morphology forming, making this assumption to be inapplicable. For investigation purposes, an equivalent diameter of droplets, D_{eff}, is adopted as the representation of droplet initial diameter [36], which is calculated by the droplet volume V as:

$$D_{eff} = \sqrt[3]{\frac{6V}{\pi}}. \quad (1)$$

From Fig. 2, when the shielding gas supply rate is low ($Q < 0.8$ L/min), droplets tend to have a larger equivalent diameter and poorer circularity. As the shielding gas supply rate increase, the droplets gradually return to a spherical shape, and the equivalent diameter decreases until it stabilizes at ~430 μm.

3.2. Analysis of droplet impact dynamic behavior under shielding gas

3.2.1. Dynamic process of single metal droplet deposition

The deposition process of unoxidized metal droplets is influenced by the coupling of dynamic and thermodynamic behaviors. There are five distinct stages for the metal droplet deposition process based on the droplet's evolution: pre-impact, spreading, recoil, oscillations, and stationary [37], as depicted in Fig. 3(a)~(e). In the pre-impact stage, a metal droplet with an initial temperature T_d and an initial velocity v_d falls through shielding gas, approaching a cold substrate with a temperature T_s. Upon contacting the substrate, the droplet enters the spreading stage. Here, the internal fluid continues to move downward under inertial force, resulting in a gradual decrease in droplet height $h(t)$ and a gradual increase in spreading diameter $d(t)$. Once the initial kinetic energy of the droplet thoroughly converts into surface energy, the

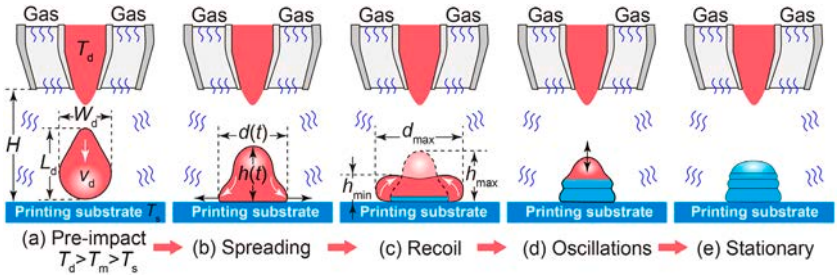

Fig. 3. Schematic diagram of five typical stages for the metal droplet deposition dynamics: (a) Pre-impact; (b) Spreading; (c) Recoil; (d) Oscillations; (e) Stationary.

spreading stops. At this time, the droplet reaches its maximum spreading diameter and minimum height. In the recoil stage, the droplet retracts upward under the effect of surface tension, leading to an increase in height and a reduction in its spreading diameter. Meanwhile, partial solidification from the bottom of the droplet upward resists further changes in the spreading diameter, while the unsolidified portion continues to recoil until it reaches the maximum height. Afterward, the droplet repeatedly oscillates with declining amplitude as it seeks to balance the remaining kinetic and surface energy. Finally, the kinetic energy of the droplet is dissipated by viscous resistance and solidification, leading to a stationary state. This concludes the droplet deposition process.

The CCD snapshots of the droplet deposition process at different shielding gas supply rates are exhibited in Fig. 4, where droplet dynamics after the second oscillation are omitted for brevity. At shielding gas flow rates below 3 L/min, the deposition dynamics are hindered by oxidation, resulting in the retention of the droplets' initial tail tip until complete solidification. As the shielding gas flow rate increases, the final solidification shape of droplets approaches a hemispherical shape due to the initial droplet shape becomes more round. In addition, there are also notable differences in droplet dynamic behavior at different shielding gas supply rates. When the shielding gas supply rate is <0.3 L/min, no apparent retraction or oscillation could be observed after the droplet spreads on the substrate, with the entire deposition process finishes within ~1 ms. As the shielding gas supply rate rises to 0.6 L/min, the droplet shows a visible recoil behavior, albeit without subsequent oscillations. However, once the shielding gas supply rate exceeds 0.9 L/min, the droplet undergoes repeated oscillations during deposition, and the time required for the droplet to reach a stationary state increases as the shielding gas supply rate continues to rise.

The visual presentation of droplet deposition process under different shielding gas supply rates is shown in the Supplementary Video 1.

3.2.2. *Spreading and recoil behaviors of metal droplets*

To quantify the dynamics of droplet impact, dimensionless parameters, including droplet spreading factor ξ, and recoil factor η, are defined

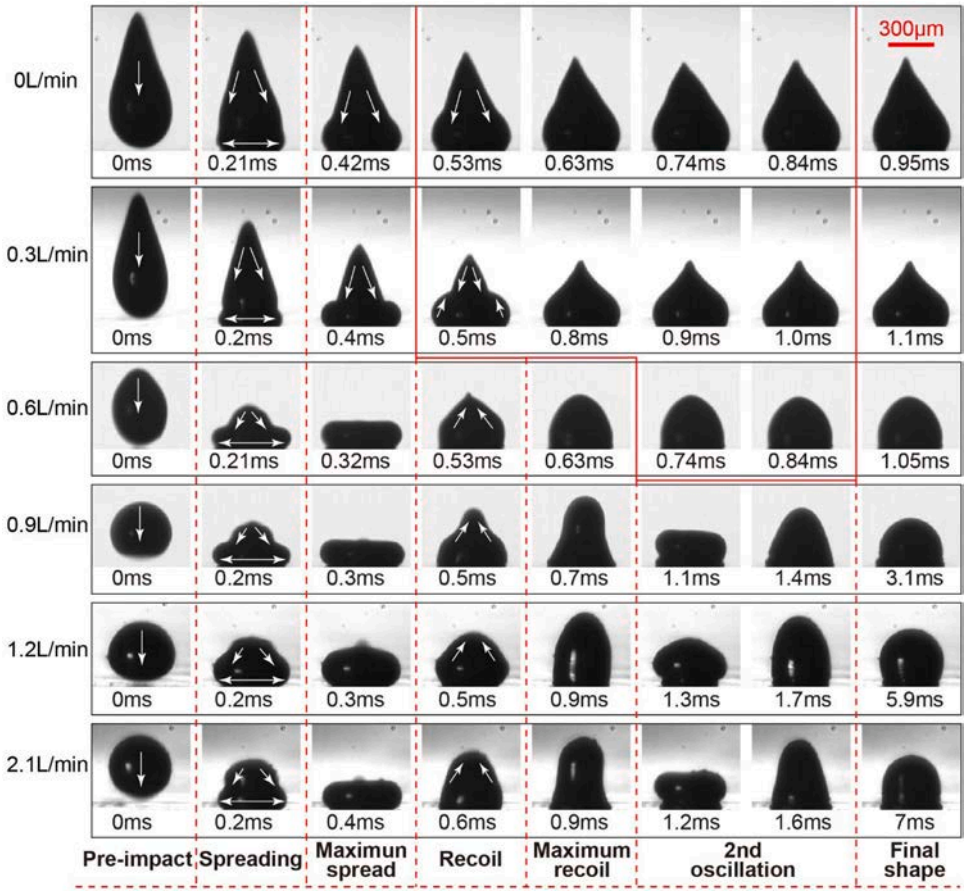

Fig. 4. CCD snapshots of the droplet deposition process under different shielding gas supply rates.

as [38]

$$\xi(t)=\frac{d(t)}{W_d},\eta(t)=\frac{h(t)}{L_d}. \tag{2}$$

The Weber number *We* and Reynolds number *Re* of droplets are used to describe the fluid flow conditions, which are

$$We=\frac{\rho {v_d}^2 D_{eff}}{\sigma},Re=\frac{\rho v_d D_{eff}}{\mu_m}. \tag{3}$$

Furthermore, Stefan number *Ste* and the Peclet number *Pe*, which are the dimensionless numbers concerning the droplet heat transfer behavior, are denoted by

$$Ste=\frac{C_m(T_m-T_{si})}{H_f},Pe=\frac{v_d D_{eff}}{\alpha_{diff}}, \tag{4}$$

where T_{si} is the substrate's initial temperature, which is ~290 K in this study. α_{diff} is the thermal diffusion coefficient defined as $\alpha_{diff}=k_m/(C_m\rho_m)$.

The maximum spreading factor and the maximum recoil factor are essential parameters to describe droplet dynamics. Numerous theoretical studies have focused on the prediction the maximum spreading factor. Pasandideh-Fard et al. [27] developed a prediction model for the droplet's maximum spreading factor based on the energy conservation model. However, since they used water as the experimental material, the model did not account for the solidification behavior during spreading. Aziz et al. [17] later introduced a model for predicting the maximum spreading factor in metal droplet deposition by incorporating solidification theory.

Nevertheless, their model treats the metal droplets in the maximum spreading state as a disk of negligible thickness, leading to an overestimation of the maximum spreading factor at low Weber numbers. In this study, the surface energy is incorporated in the droplet thickness direction into the primary energy term, thereby establishing a more accurate droplet impact dynamics modeling for MDDM.

Before the droplet spreading starts, the total energy mainly consists of the initial kinetic energy E_{k0} and the initial surface energy E_{s0} [17]:

$$E_{k0}=\frac{1}{12}\pi\rho {D_{eff}}^3 {v_d}^2, \tag{5}$$

$$E_{s0}=\pi {D_{eff}}^2\sigma. \tag{6}$$

At the moment of the droplet's maximum spreading, its kinetic energy diminishes to zero, leaving its total energy primarily as surface energy E_{s1}. Assuming the droplet at the maximum spreading forms a regular disk, the total surface energy E_{s1} could be calculated by the sum of the energy from the upper surface and the side surface as [39]

$$E_{s1}=\frac{\pi}{4}{d_{max}}^2\sigma(1-\cos\theta_a)+\frac{2\pi}{3}\frac{{D_{eff}}^3}{d_{max}}\sigma, \tag{7}$$

where θ_a is the advancing contact angle of the droplet, which can be measured by the CCD snapshot of the droplet spreading. d_{max} is the maximum spreading diameter.

The viscous dissipation energy E_{v1} during the droplet spreading to its maximum diameter could be expressed as [27]

$$E_{v1}=\frac{\pi}{8\sqrt{Re}}\rho {v_d}^3 {d_{max}}^2 t_s, \tag{8}$$

where t_s is the droplet spreading time. Chandra et al. [40] suggested that $t_s=D_{eff}/v_d$, which is closer to the droplet spreading time in this study, thus

$$E_{v1}=\frac{\pi}{8}{d_{max}}^2\sigma\frac{We}{\sqrt{Re}}. \tag{9}$$

Additionally, part of kinetic energy is lost due to droplet solidification. When the thickness of the solidification layer is *s*, the kinetic energy lost ΔE_1 is [41]

$$\Delta E_1=\frac{\pi}{32}\rho {d_{max}}^2 {v_d}^2 s. \tag{10}$$

The thickness of the solidification layer *s* could be denoted as

$$s=\sqrt{2t^*\frac{Ste}{Pe}}. \tag{11}$$

t^* is the dimensionless time. Here it is taken as 1.

Further, balancing the total energy before the droplet reaches its maximum spreading diameter, that is

$$E_{k0}+E_{s0}=E_{s1}+E_{v1}+\Delta E_1. \tag{12}$$

From Eqs. (5)~(7) and (9)~(12), inferring

$$\left(\frac{d_{max}}{D_{eff}}\right)^3+P\frac{d_{max}}{D_{eff}}+Q=0. \tag{13}$$

Here, $P=-\frac{4(We+12)}{3We\sqrt{\frac{Ste}{2Pe}}+12(1-\cos\theta_a)+6\frac{We}{\sqrt{Re}}}$, $Q=\frac{32}{3We\sqrt{\frac{Ste}{2Pe}}+12(1-\cos\theta_a)+6\frac{We}{\sqrt{Re}}}$.

The maximum spreading factor could be obtained by solving the Cardano formula as

$$\xi_{max}=\left(\sqrt[3]{-\frac{P_2}{2}+\sqrt{\frac{{P_1}^3}{27}+\frac{{P_2}^2}{4}}}+\sqrt[3]{-\frac{P_2}{2}-\sqrt{\frac{{P_1}^3}{27}+\frac{{P_2}^2}{4}}}\right)D_{eff}\Big/W_d. \tag{14}$$

For pure tin alloy droplets, the Weber number is ~5.3, the Reynolds number is ~1522, and the calculated maximum spreading factor is about 1.3096. Fig. 5 shows the droplets' maximum spreading factor and the maximum recoil factor at different shielding gas supply rates. The theoretical value of the maximum spreading factor, derived from Eq. (14), shows different prediction accuracy depending on the initial droplet shapes. For spherical droplets, when the shielding gas supply rate exceeds 0.8 L/min, the theoretical value of the maximum spreading factor aligns closely with the experimental results. However, for non-spherical droplets, the theoretical maximum spreading factor deviates from the practical value, with the deviation increasing as the shielding gas supply rate decreases. This discrepancy at lower shielding gas supply rates may be attributed to oxidation effects. When the shielding gas flow is insufficient, the droplets are not fully shielded from exposure to oxygen in the surrounding atmosphere. The oxidation effect changes the droplet's physical properties, such as surface tension and viscosity, making the model for predicting the maximum spreading factor inapplicable.

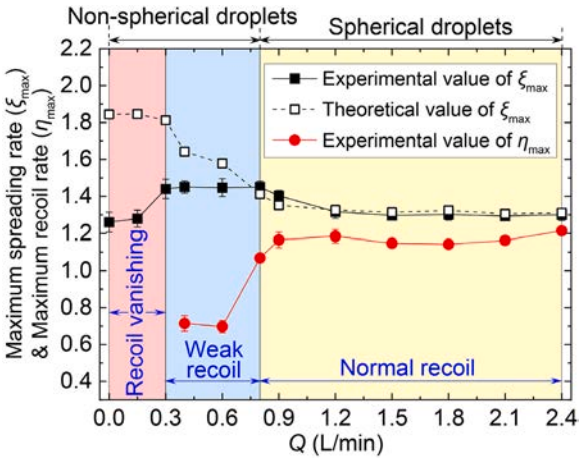

Fig. 5. Maximum spreading factor and maximum recoil factor of droplets at different shielding gas supply rates.

Extensive research has been conducted on the effects of oxidation on the physical properties of metal droplets. Present studies have demonstrated that different detection methods could induce dramatic variations in surface tension measurements of the oxidized liquid metal. Taimatsu et al. [42] and Yuan et al. [43] employed the sessile drop method to measure the surface tension of oxidized molten tin, finding that the oxidized droplet showed with a better wettability on the substrate. They concluded that oxidation would decrease the surface tension. Conversely, Xu et al. [44] used the pendant drop method to measure the surface tension of liquid gallium, discovering that the oxidized film introduced yield stress. The oxidized liquid metal exhibited a solid-like elastic response under low applied stress, thereby increasing the measured surface tension. The differing results from these two methods stem from the mechanical stress effects of the oxide film. In the sessile drop method, the oxide film limits the release of droplet surface energy, reducing the contact angle. In the pendant drop method, the mechanical stress of the oxide film superimposes with the surface tension, collectively inhibiting the droplet from falling off. For this study, the conclusion from the pendant drop method is more representative, as the oxide mechanical stress and the surface tension act together to hinder droplet deformation together during its spreading. Besides, Xu et al. [44] and Patouillet et al. [45] measured the viscosity of molten gallium alloys and aluminum alloys, respectively. It was found that the oxide film would continuously breaks and forms under the shear force, inducing the melt to exhibit non-Newtonian fluid behavior with the shear-thinning property. The oxidized melt demonstrates high viscosity. As the shear rate increases, the viscosity of the oxidized melt decreases and gradually approaches the viscosity of pure melt at high shear rates. From Eq. (14), an increase in either surface tension or viscosity would decrease the maximum spreading factor of the droplet. The mechanical stress of the oxide film dissipates partial energy during the conversion between droplet kinetic energy and surface tension. Therefore, the experimental value of the maximum spreading factor is smaller than the theoretical value at lower shielding gas supply rates.

According to the maximum recoil factor scale, droplets exhibit three different recoil behaviors at different shielding gas supply rates (Fig. 5): recoil vanishing, weak recoil, and normal recoil. The vanishing and weakening of the recoil behavior occurs only during the deposition of non-spherical droplets, indicating that oxidation induces abnormal droplet recoil behavior. Affected by oxidation, the droplet's surface becomes covered by an oxide film before impacting the substrate (Fig. 6(a)). During the spreading process, the droplet's deformation stretches and tears the surface oxide film, exposing fresh tin melt (Fig. 6(b)). As the droplet continues to spread and deform, the increasing surface area creates additional breaks in the oxide layer. The tin melt exposed by the previous breaks is reoxidized until the droplet reaches its maximum spreading diameter, as illustrated in Fig. 6(c). At the maximum spreading state, a significant increase in viscosity occurs due to the shear-thinning property of the oxidized metal fluid, as the droplet's kinetic energy is minimized. This increased viscosity leads to greater viscous dissipation during retraction and recoil, thereby weakening or eliminating the recoil phenomenon (Fig. 6(d)).

3.2.3. Oscillation behavior of metal droplets

Taking the instant of contact between the droplet and the substrate as the initial moment, the evolution of the droplet spreading factor ξ and recoil factor η over the deposition time could be acquired from the CCD snapshot, as shown in Fig. 7(a) and (b).

From Fig. 7(a), metal droplets at different shielding gas supply rates reach the maximum spreading stage around 0.3 to 0.4 ms. At a shielding gas supply rate of 0.3 L/min, the droplet retracts slightly after reaching its maximum spreading due to the oxide film limiting, resulting in a final spreading factor of ~1.39. As the shielding gas supply rate increases and the oxidation effect weakens, the frequency of droplet's spreading and retraction increases significantly. This enhanced retraction leads to a final stable spreading factor of around 1.05. Besides, the droplet recoil factor at different shielding gas supply rates follows a rule similar to the spreading factor, as shown in Fig. 7(b). At a shielding gas supply rate of 0.3 L/min, no noticeable droplet recoil, causing a final droplet recoil factor of ~0.54. As the shielding gas supply rate increases, both the frequency and amplitude of droplet oscillations intensify, and the recoil factor stabilizes at ~0.92 when the droplet becomes fully stationary.

The oscillation times and the oscillation duration of droplets at different shielding gas supply rates are summarized in Fig. 8. The droplet oscillation behavior is divided into three stages: oscillation vanishing, oscillation recovering, and normal oscillation. When the shielding gas supply rate is below 0.3 L/min, the droplet oscillation behavior vanishes completely, and the time taken for the droplet to reach a stationary state is minimized. In the oscillation recovering phase, both the oscillation times and the oscillation duration increase linearly due to the recovery of droplet's surface tension. After the shielding gas supply rate reaches 1.8 L/min, the droplet oscillation times stabilizes at ~17, while the oscillation duration remains ~7 ms. From SEM images in Fig. 8, the solidified droplet forms a sharp tip when the shielding gas supply rate is low, due to the initial droplet morphology featuring a tapered tail. As the shielding gas supply rate increases, the tip gradually disappears with the restoration of the droplet's spherical morphology. Meanwhile, the increased number of oscillations at higher shielding gas supply rate produces more surface oscillation ripples on the final droplet.

To verify the formation of oxide film, EDS analysis was performed on the cross-sectional of the droplet. The Schematic diagram of the EDS point position and line scan path are shown in Fig. 9(a). For the EDS sampling points, Point 1 was selected near the droplet's edge, and Point 2 was chosen farther away from the edge. As a shielding gas supply rate of 0.15 L/min, the corresponding EDS spectra from these sampling points are shown in Fig. 9(b) and (c). It could be seen that the oxidation at the droplet surface leads to a high O level at Point 1, while the detected O weight percentage at Point 2 is extremely low due to its distance from the surface. For the EDS line scan, the EDS path begins from the droplet edge and scans inward the droplet. The normalized distribution data for Sn and O at different shielding gas supply rates are shown in Fig. 9(d)~(i). When the shielding gas supply rate is lower than 1.5 L/min, oxidation of the droplet induces a high O level at the scan path beginning, demonstrating that the oxide film is formed on the droplet surface. The thickness of the oxide film does not exceed 1 μm. As the shielding gas supply rate increases, the weakening oxidation effect

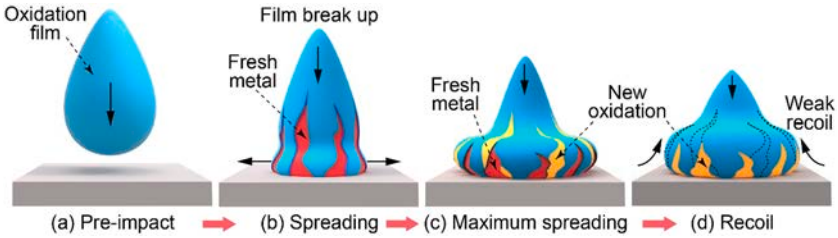

Fig. 6. Schematic diagram for the effect of oxide film breakup and generation on the molten droplet deposition at different stages: (a) Pre-impact; (b) Spreading; (c) Maximum spreading; (d) Recoil.

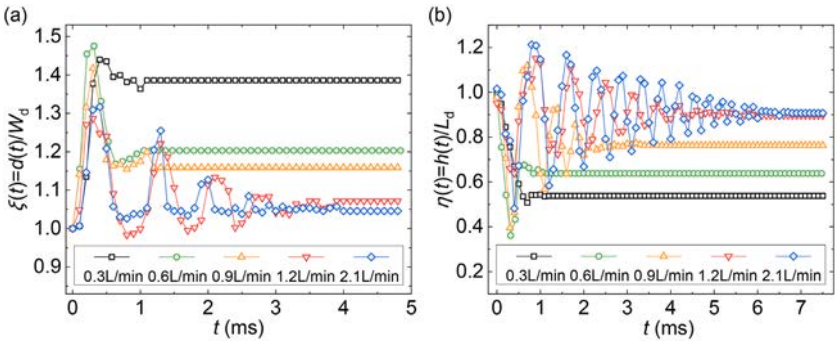

Fig. 7. Variation of (a) spreading factor and (b) recoil factor during droplet oscillation under different shielding gas supply rates.

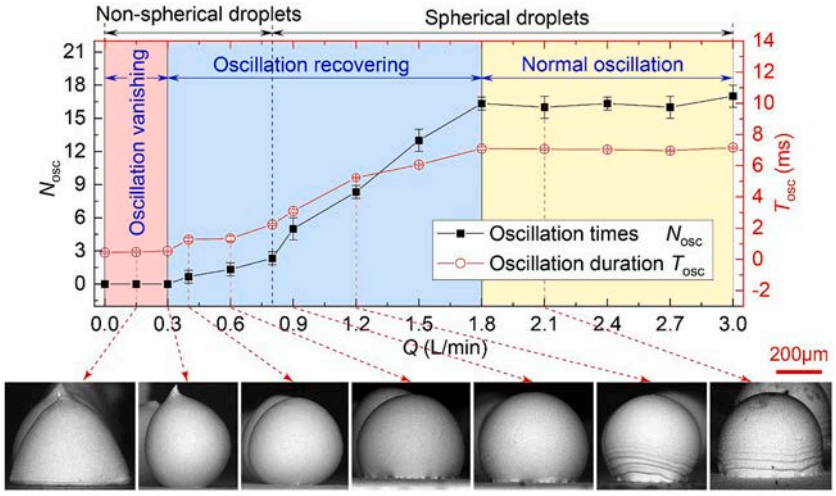

Fig. 8. Droplet oscillation behavior characterization and solidification morphologies under different shielding gas supply rates.

narrows the region with high O level. When the shielding gas supply rate is higher than 1.5 L/min, the high O region on the droplet surface almost disappears, indicating further thinning of the oxide film.

Moreover, as shown in Figs. 8 and 9, when the shielding gas supply rate exceeds 0.8 L/min, the droplet tends to form a spherical shape due to the weakening oxidation effect and the surface tension recovery. However, within the range of 0.8~1.8 L/min, not only are the oscillation times and oscillation duration smaller than those of normal droplet oscillation, but the presence of an oxide film could also be detected at the droplet interface. Interestingly, the threshold for the droplet forming a spherical does not align with the threshold for normal oscillation behavior. It suggests that relying solely on the initial tail morphology to evaluate the droplet's oxidation status may be insufficiently accurate, even though this more intuitive approach is commonly adopted in most literature.

3.3. Effect of droplet impact dynamic behavior on its overlapping fusion quality

3.3.1. Dynamic process of metal droplet overlapping

The overlapping of two droplets is a fundamental process in MDDM. As discussed earlier, droplet deposition dynamics and deposition morphology under shielding gas vary significantly, making the droplet's overlapping behavior and fusion quality unpredictable. The adjacent droplet overlapping process, illustrated in Fig. 10, includes the processes of pre-overlap, spreading, recoil, oscillations, and stationary. This process is similar to that of single droplet deposition, except that the direction of the second droplet spreading and oscillation would be affected by the previous droplet.

To further investigate droplet overlapping dynamics, the instant of droplet overlapping begins is taken as the initial moment. The total width of the two droplets at this moment is defined as the initial overlapping width L_0, while the height of the first deposited droplet is referred to as the initial overlapping height H_{s1}. During the subsequent stages of droplet spreading, recoil, and oscillations, the height of the flowing front for the second droplet H_2, and the total overlapping length L, keep changing over time t. As the second droplet's kinetic energy dissipates, it solidifies into a bump with a height of H_{s2}, fusing with the first droplet to a final overlapping length of L_s. Moreover, droplet dimensionless overlapping length β_L and dimensionless overlapping height β_H are defined by referencing the second droplet's oscillation front, which are

$$\beta_L = \frac{L(t)}{L_0}, \beta_H = \frac{H_2(t)}{H_{s1}}. \tag{15}$$

A closer value of β_L and β_H to 1 indicates a decrease in both the droplet overlapping length error and height error, thereby reflecting a better droplet overlapping quality.

The droplet overlapping process is mainly influenced by the combined effect of the printing step distance and the shielding gas supply rate. Fig. 11(a) shows the CCD snapshots of the droplet overlapping process at different printing step distances L and shielding gas supply rates Q. The variation of dimensionless overlapping length β_L and height β_H over time t is statistically plotted in Fig. 11(b). In comparison, when the printing step distance is 0.24 mm, the dimensionless overlapping length is greater, and the oscillation amplitude and the oscillation times of β_L are significantly higher than those at step distances of 0.32 mm and 0.44 mm (Fig. 11(b)). From the CCD snapshots in Fig. 11(a), at a small

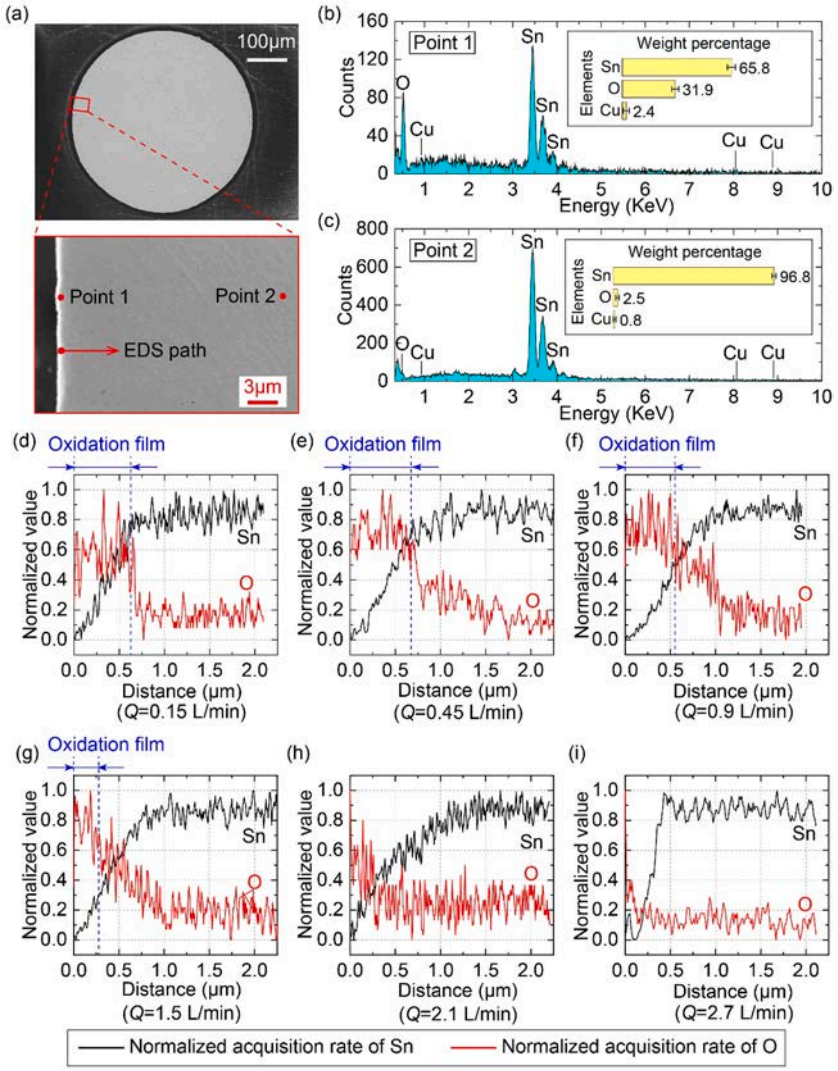

Fig. 9. EDS analysis of tin alloy droplets. (a) Schematic diagram of EDS point position and line scan path; EDS point analysis for (b) Point 1 and (c) Point 2 when the shielding gas supply rate is 0.15 L/min, the respective EDS spectra obtained at sampling points are shown in Fig. 9(b) and (c); Distribution data for Sn and O at shielding gas supply rate of (d) 0.15 L/min, (e) 0.45 L/min, (f) 0.9 L/min, (g) 1.5 L/min, (h) 2.1 L/min, and (i) 2.7 L/min.

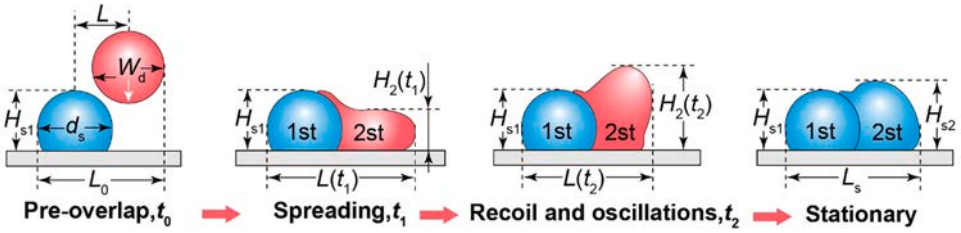

Fig. 10. Schematic diagram for characterizing the droplet overlapping process.

printing step distance, the second droplet prematurely contacts and impacts with the first droplet during overlapping, sliding down along the side of the first droplet until it settles onto the substrate. The existence of the first droplet redirects the second droplet's movement, inducing most of its kinetic energy to dissipate horizontally. With the increase of the printing step distance, the influence of the first droplet on the second droplet's overlapping behavior weakens. Consequently, the amplitude and number of oscillations in the dimensionless overlapping length decrease, while those in the dimensionless overlapping height increase (Fig. 11(b)). When L is 0.44 mm, the longer printing step distance allows the second droplet to first contacts the substrate and overlaps with the first droplet as it spreads (Fig. 11(a)). In this case, the second droplet's kinetic energy dissipates mainly in the vertical direction, similar to the single droplet deposition behavior.

As a shielding gas supply rate of 0.6 L/min, oxidation prevents the second droplet from retracting or recoiling after reaching its maximum spreading state. Such a phenomenon is especially evident at small printing step distances, leading to a greater dimensionless overlapping length, smaller dimensionless overlapping height, and poorer overlapping morphology. As the shielding gas supply rate increases, the droplet's recoil and oscillation behavior gradually recover due to the weakening oxidation. Correspondingly, there is a decrease in

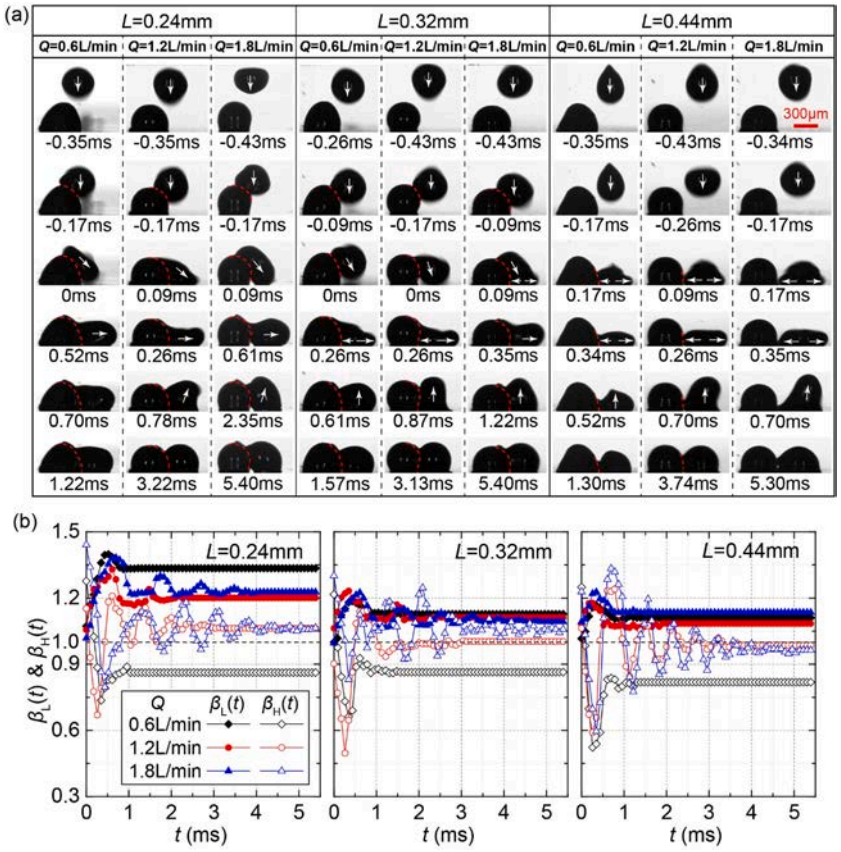

Fig. 11. Droplet overlapping process at different printing step distances and shielding gas supply rates. (a) CCD snapshots; (b) Variation of the droplet dimensionless overlapping length and the dimensionless overlapping height.

dimensionless overlapping length, an increase in dimensionless overlapping height, and an improvement in droplet overlapping accuracy. This indicates that appropriately increasing the shielding gas supply rate and the printing step distance could enhance the droplet overlapping accuracy.

The visual presentation of droplet overlapping process at different printing step distances and shielding gas supply rates is shown in the Supplementary Video 2.

3.3.2. *Metal droplet overlapping fusion quality under shielding gas*

The accumulation of the overlapping tolerance during the droplet deposition process would negatively affect the printed morphology and dimensions, making it crucial to minimize droplet overlapping tolerance as much as possible. Based on the above investigations, the drawback index of overlapping length, ψ_L, and the drawback index of overlapping height, ψ_H, are defined to quantify the droplet overlapping accuracy, which are

$$\psi_L = \left|\frac{L(t) - L_0}{L_0}\right|, \psi_H = \left|\frac{H_2(t) - H_{s1}}{H_{s1}}\right|. \quad (16)$$

A closer ψ_L and ψ_H to zero indicates a better overlapping accuracy, while a larger ψ_L and ψ_H means a higher error in the overlapping length and the overlapping height.

To further clarify the parameters for achieving high-quality droplet overlapping under coaxial shielding gas, the fusion quality of droplet overlapping was statistically analyzed within a range of the shielding gas supply rate from 0.3 to 1.8 L/min and the printing step distance from 0.2 to 0.44 mm. Fig. 12(a) exhibits binarized CCD maps of the droplet overlapping morphology under different deposition conditions. Fig. 12 (b) and (c) illustrate heat maps corresponding to the drawback index for overlapping length and overlapping height. In the heat maps, colors closer to blue indicate better quality overlapping, while colors closer to red signify poorer quality overlapping.

From Fig. 12(b) and (c), it is evident that smaller printing step distances result in worse drawback indices for both overlapping length and height, as the previously solidified droplet interferes with the deposition behavior of the second droplet. Additionally, there is also a declined droplet overlapping fusion quality caused by lower shielding gas supply rates, as oxidation weakens the droplet's retraction behavior. Increasing the shield gas supply rate and the printing step distance effectively improves droplet overlapping fusion quality. However, if the printing step distance is too large (e.g., L = 0.44 mm), a poor or broken connection between the droplets would occur. To achieve high-accuracy droplet overlapping in an opening environment, the shielding gas supply rate should be kept above 1.2 L/min, and the printing step distance should fall between 0.28~0.4 mm (with an overlapping factor L/D_{eff} of about 0.65 to 0.93). The blue wireframe in Fig. 12(a) shows the ideal droplet overlapping morphology, where the drawback index of overlapping length is <0.15, and the drawback index of overlapping height is below 0.05.

By longitudinally dissecting the droplet overlapping sample at the ideal overlapping parameter from Fig. 12(a), the interior morphology SEM image of droplet overlapping was obtained, as shown in Fig. 13(a). No apparent cold laps or pores are visible in the droplet remelting zone, indicating that good fusion between droplets could be realized under these parameters. An EDS line scan analysis was performed across the remelting zone along the path shown in Fig. 13(a), and the corresponding EDS spectrum (Fig. 13(b)) and element distribution (Fig. 13 (c)) for Sn and O were obtained. An extremely low weight percentage of O was detected in the overlapping region, with no abrupt variations in Sn and O distribution along the scan path. Additionally, metallographic etching was conducted for the droplet of Fig. 13(a), as shown in Fig. 13

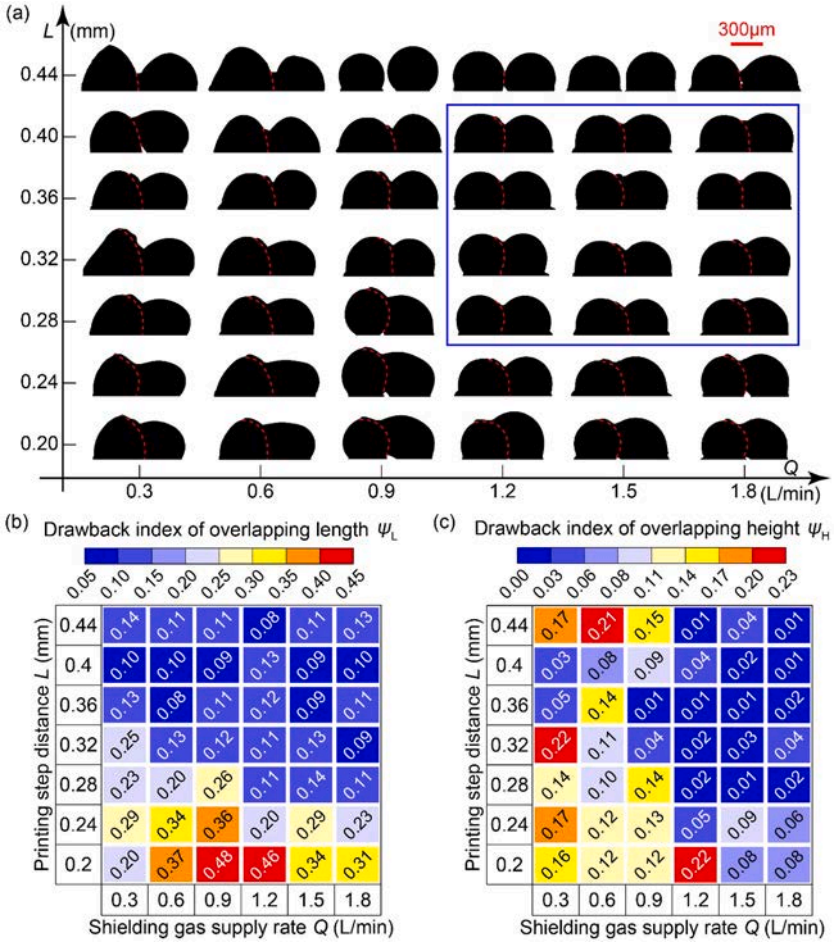

Fig. 12. Characterization of droplet overlapping quality for different printing step distances and shielding gas supply rates. (a) Binarized CCD maps of droplet overlapping morphology; (b) Drawback index of overlapping length; (c) Drawback index of overlapping height.

(d). Influenced by the solidification direction, the grain growth direction of the two droplets is inconsistent. Near the remelting zone, dendritic structures of the previous deposition droplet grow vertically, while those of the later droplet grow horizontally. Inside the remelting zone, a clear droplet fusion line and dense grain structures are visible, reflecting the intergranular bonding between the two droplets, which confirms that metallurgical bonding could be achieved under these parameters.

4. Conclusions

In this work, aiming to achieve the high-quality metal droplet overlapping fusion in an opening environment, a strategy to suppress metal droplet overlapping fusion defects in CSG-based MDDM was proposed for the first time. By combining high-speed photography, droplet deposition experiments, and theoretical modeling, an improved prediction model for the maximum spreading factor of molten droplets was constructed. Additionally, the evolution of the metal droplet spreading, oscillation, and overlapping behaviors under coaxial shielding gas was studied insightfully. The result shows that the constructed droplet maximum spreading factor model closely aligns with experimental values at higher shielding gas supply rates. However, when the shielding gas supply rate is lower, the actual maximum spreading factor is significantly reduced compared to the theoretically predictions. This reduction is attributed to the self-limiting effect of the oxide film on the droplet surface, where the increasing equivalent surface tension and the shear-thinning property of the oxidized droplet weaken or eliminate the droplet retraction, recoil, and oscillation behaviors. Furthermore, it is found that a greater dimensionless overlapping length, smaller dimensionless overlapping height, and poorer overlapping quality occur when the second droplet's retraction is weakened at low shielding gas supply rates. Such a phenomenon is particularly evident when the printing step distance is small, as the previously solidified droplet alters the kinetic energy dissipation direction of the second droplet. Finally, a droplet overlapping quality map was established for different deposition parameters, and a strategy for controlling droplet overlapping accuracy in an opening environment was proposed. When the shielding gas supply rate exceeds 1.2 L/min and the overlapping factor falls between 0.65 and 0.93, fusion defects could be effectively suppressed, allowing for metallurgical bonding between droplets and ensuring high fusion quality at the microstructural level. This work may provide theoretical guidance for achieving high-quality formation in CSG-based MDDM, contributing to the industrial development and application of related technologies.

CRediT authorship contribution statement

Yi Zhou: Conceptualization, Formal analysis, Data curation, Investigation, Methodology, Software, Validation, Writing – original draft. **Jun Luo:** Project administration, Funding acquisition. **Lin Su:** Investigation. **Lehua Qi:** Methodology, Writing – review & editing, Supervision, Project administration, Funding acquisition.

Declaration of competing interest

The authors declare that they have no known competing financial interests or personal relationships that could have appeared to influence

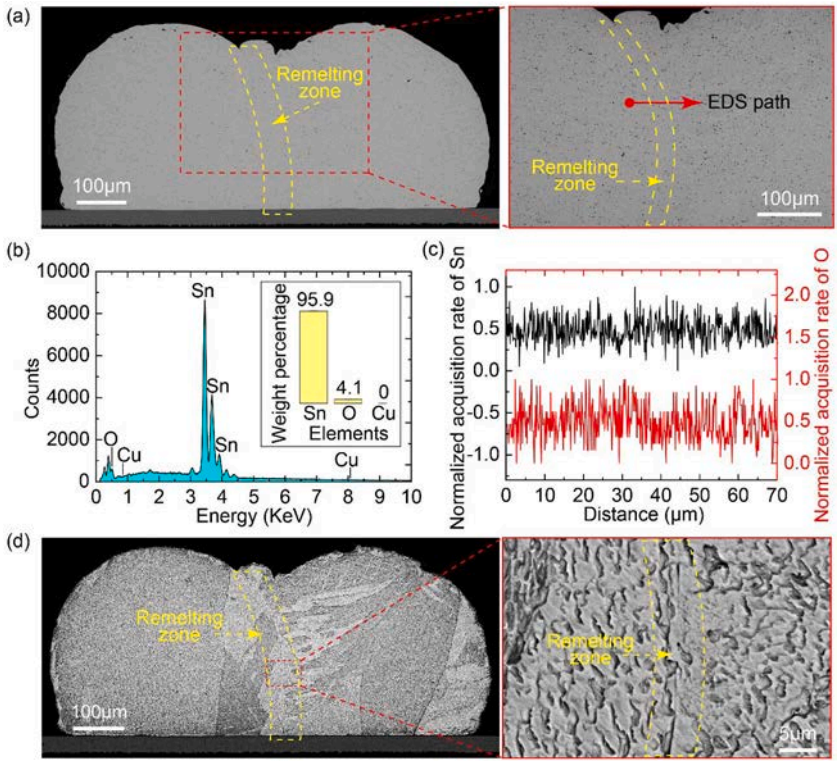

Fig. 13. Droplet fusion quality under ideal overlapping parameter. (a) Droplet interior SEM morphology; (b) EDS spectrum for scan path in (a); (c) Distribution data of Sn and O for scan path in (a); and (d) Metallographic of the two overlapping droplets in (a).

the work reported in this paper.

Acknowledgements

This work was supported by the National Natural Science Foundation of China (No. 52231004); the Natural Science Basic Research Program (Excellent Youth Foundation) of Shaanxi (No. 2024JC-JCQN-56).

Supplementary materials

Supplementary material associated with this article can be found, in the online version, at doi:10.1016/j.ijheatmasstransfer.2024.126488.

References

[1] T.Y. Ansell, Current status of liquid metal printing, J. Manuf. Mater. Process. 5 (2021) 31.
[2] M. Ma, X.F. Wei, X.Y. Shu, H.H. Zhang, Producing solder droplets using piezoelectric membrane-piston-based jetting technology, J. Mater. Process. Technol. 263 (2019) 233–240.
[3] D. Lu, F.M. Xu, L. Zhao, Y.F. Fu, W. Dong, Y. Tan, A. Kawasaki, Fabrication of BGA Solder Balls By Pulsated Orifice Ejection Method, IEEE, Piscataway, NJ, 2013, pp. 694–697.
[4] C.J. Zhang, Q. Yang, J.L. Yong, C. Shan, J.Z. Zhang, X. Hou, F. Chen, Guiding magnetic liquid metal for flexible circuit, Int. J. Extreme Manuf. 3 (2021) 025102.
[5] M. Meda, P. Mehta, C. Mahajan, B. Kahn, D. Cormier, Magnetohydrodynamic liquid metal droplet jetting of highly conductive electronic traces, Flex. Print. Electron. 6 (2021) 035002.
[6] S.L. Li, Z.Y. Wei, J. Du, G.X. Zhao, X. Wang, B.H. Lu, Numerical and experimental investigation of molten metal droplet deposition applied to rapid prototyping, Appl. Phys. A Mater. Sci. Process. 122 (2016) 1–5.
[7] Y.P. Chao, A novel selection method of slice thickness in metal micro-droplet deposition manufacture, J. Manuf. Process. 21 (2016) 153–159.
[8] G. Luo, D. Wu, Y. Zhou, Y. Hu, Z. Yao, Laser printing of large-scale metal micro/nanoparticle array: deposition behavior and microstructure, Int. J. Mach. Tools Manuf. 173 (2022) 103845.
[9] Y. Nakata, E. Hayashi, K. Tsubakimoto, N. Miyanaga, A. Narazaki, T. Shoji, Y. Tsuboi, Nanodot array deposition via single shot laser interference pattern using laser-induced forward transfer, Int. J. Extreme Manuf. 2 (2020) 025101.
[10] E. Govekar, A. Jeromen, A. Kuznetsov, M. Kotar, M. Kondo, Annular laser beam based direct metal deposition, Procedia CIRP 74 (2018) 222–227.
[11] H. Merrow, J.D. Beroz, K. Zhang, U.P. Muecke, A.J. Hart, Digital metal printing by electrohydrodynamic ejection and in-flight melting of microparticles, Addit. Manuf. 37 (2021) 101703.
[12] H. Yi, J. Li, Z. Wang, H. Cao, M. Liu, Elimination of gas entrapment in droplet-based 3D printing by induced electric-field, Int. J. Mech. Sci. 266 (2024) 108974.
[13] Y. Zhou, L.H. Qi, J. Luo, S. Lin, Investigation on the effect mechanism of micro-domain shielding gas on metal droplet ejection process, J. Mech. Eng. 59 (2023) 219–230. Chinese.
[14] X.X. Yao, J.Y. Li, Y.F. Wang, X. Gao, T. Li, Z. Zhang, Experimental and numerical studies of nozzle effect on powder flow behaviors in directed energy deposition additive manufacturing, Int. J. Mech. Sci. 210 (2021) 106740.
[15] A. Amirzadeh, M. Raessi, S. Chandra, Producing molten metal droplets smaller than the nozzle diameter using a pneumatic drop-on-demand generator, Exp. Therm. Fluid. Sci. 47 (2013) 26–33.
[16] J.M. Waldvogel, D. Poulikakos, D.B. Wallace, R. Marusak, Transport phenomena in picoliter size solder droplet dispension, J. Heat Transf. 118 (1996) 148–156.
[17] S.D. Aziz, S. Chandra, Impact, recoil and splashing of molten metal droplets, Int. J. Heat Mass Transf. 43 (2000) 2841–2857.
[18] B. Xiong, C.M. Megaridis, D. Poulikakos, H. Hoang, An investigation of key factors affecting solder microdroplet deposition, J. Heat Transf. 120 (1998) 343–350.
[19] S. Schiaffino, A.A. Sonin, Molten droplet deposition and solidification at low Weber numbers, Phys. Fluids 9 (1997) 3172–3187.
[20] Q. Xu, V. Gupta, E. Lavernia, Thermal behavior during droplet-based deposition, Acta Mater. 48 (2000) 835–849.
[21] L.H. Qi, Y.P. Chao, J. Luo, J.M. Zhou, X.H. Hou, H.J. Li, A novel selection method of scanning step for fabricating metal components based on micro-droplet deposition manufacture, Int. J. Mach. Tools Manuf. 56 (2012) 50–58.
[22] H. Yi, L.H. Qi, J. Luo, D.C. Zhang, H.J. Li, X.H. Hou, Effect of the surface morphology of solidified droplet on remelting between neighboring aluminum droplets, Int. J. Mach. Tools Manuf. 130 (2018) 1–11.
[23] Y. Dou, J. Luo, L. Qi, H. Lian, X. Hou, Generation mechanism and suppression method of landing error of two successively deposited metal droplets caused by coalescence and solidification, Int. J. Heat Mass Transf. 172 (2021) 121100.
[24] W. Yang, R. Yang, Y. Yao, Z. Gao, H. Zhang, Effects of surface oxide layer on the impact dynamic behavior of molten aluminum droplets, Phys. Fluids 35 (2023) 013109.
[25] D. Jia, D. Zhou, P. Yi, C. Zhang, J. Li, Y. Guo, S. Zhang, Y. Li, Splat deposition stress formation mechanism of droplets impacting onto texture, Int. J. Mech. Sci. 266 (2024) 109002.
[26] Q. Xu, E. Brown, H.M. Jaeger, Impact dynamics of oxidized liquid metal drops, Phys. Rev. E 87 (2013) 043012.
[27] M. Pasandideh-Fard, Y. Qiao, S. Chandra, J. Mostaghimi, Capillary effects during droplet impact on a solid surface, Phys. Fluids 8 (1996) 650–659.

[28] R. McGuan, R.N. Candler, H.P. Kavehpour, Spreading and contact-line arrest dynamics of impacting oxidized liquid-metal droplets, Phus. Rev. Fluids 6 (2021) L111601.
[29] T. An, H. Chen, Y. Wang, H. Fang, Effect of substrate temperature on the deformation of liquid metal droplets during spreading and solidification, Int. J. Heat Mass Transf. 223 (2024).
[30] Z. Ning, H. Ming-Liang, M. Hai-Tao, P. Xue-Min, L. Xiao-Ying, Viscosities and wetting behaviors of Sn-Cu solders, Acta Phys. Sin. 62 (2013) 086601. Ch. Ed.
[31] T. Chellaih, G. Kumar, K.N. Prabhu, Effect of thermal contact heat transfer on solidification of Pb–Sn and Pb-free solders, Mater. Des. 28 (2007) 1006–1011.
[32] M.J. Assael, A. Chatzimichailidis, K.D. Antoniadis, W.A. Wakeham, M.L. Huber, H. Fukuyama, Reference Correlations For the Thermal Conductivity of Liquid Copper, Gallium, Indium, Iron, Lead, Nickel and Tin, 46, High Temperatures High Press, 2017, p. 391.
[33] T.W. Chapman, The heat capacity of liquid metals, Mater. Sci. Eng. 1 (1966) 65–69.
[34] Y. Zhou, L. Qi, H. Lian, J. Luo, L. Su, Effect of impinging behavior between annular jet shielding gas and printing substrate on metal droplet stable ejection, Addit. Manuf. 84 (2024) 104088.
[35] H. Li, S. Mei, L. Wang, Y. Gao, J. Liu, Splashing phenomena of room temperature liquid metal droplet striking on the pool of the same liquid under ambient air environment, Int. J. Heat Fluid Flow 47 (2014) 1–8.
[36] C. Zhang, L. Li, Z. Li, H. Chang, J. Liu, Investigation on the spreading and solidification of supercooled gallium droplets during impact, Int. J. Heat Mass Transf. 183 (2022) 122142.
[37] N. Gilani, N.T. Aboulkhair, M. Simonelli, M. East, I.A. Ashcroft, R.J.M. Hague, From impact to solidification in drop-on-demand metal additive manufacturing using MetalJet, Addit. Manuf. 55 (2022) 102827.
[38] L. Xia, F. Chen, T. Liu, D. Zhang, Y. Tian, D. Zhang, Phase-field simulations of droplet impact on superhydrophobic surfaces, Int. J. Mech. Sci. 240 (2023) 107957.
[39] W.K. Hsiao, Effects of surface properties on solder bump formation by direct droplet deposition, Diss. MIT. (2004) 34–35.
[40] S. Chandra, C.T. Avedisian, On the collision of a droplet with a solid surface, Proc. R. Soc. Lond. Ser. A 432 (1997) 13–41.
[41] M. Pasandideh-Fard, R. Bhola, S. Chandra, J. Mostaghimi, Deposition of tin droplets on a steel plate: simulations and experiments, Int. J. Heat Mass Transf. 41 (1998) 2929–2945.
[42] H. Taimatsu, R. Sangiorgi, Surface tension and adsorption in liquid tin-oxygen system, Surf. Sci. 261 (1992) 375–381.
[43] Z.F. Yuan, K. Mukai, K. Takagi, M. Ohtaka, W.L. Huang, Q.S. Liu, Surface tension and its temperature coefficient of molten tin determined with the sessile drop method at different oxygen partial pressures, J. Colloid Interface Sci. 254 (2002) 338–345.
[44] Q. Xu, N. Oudalov, Q. Guo, H.M. Jaeger, E. Brown, Effect of oxidation on the mechanical properties of liquid gallium and eutectic gallium-indium, Phys. Fluids 24 (2012) 299–606.
[45] K. Patouillet, L. Davoust, Between no slip and free slip: a new boundary condition for the surface hydrodynamics of a molten metal, Chem. Eng. Sci. 231 (2020) 116328.